Chapter 13 Photon Collider

1 Introduction

The concept of producing $\gamma\gamma$ collisions through Compton backscattering of laser photons in a linear collider [1,2] was proposed in 1981. The available laser technology was barely adequate for the accelerators operating at that time. The linear colliders proposed since then are orders of magnitude more ambitious and require equivalent improvements in laser technology to produce a $\gamma\gamma$ collider. Fortunately, breakthroughs in laser technology have made feasible lasers capable of delivering the 10 kW of average power in short pulses of 1 TW peak power that are required for the NLC. The problem of obtaining such high peak power was resolved in 1985 with the invention of Chirped-Pulse Amplification (CPA). The high average power requirement could not be met without a long technology campaign that involved the development of diode-pumped lasers, adaptive optics and high-power multilayer optics, plus all of the associated engineering for thermal management. Nevertheless, today the laser and optics technology is finally in hand to proceed with an engineering design of a photon collider.

In the past few years there has been a crescendo of interest and theoretical activity in $\gamma\gamma$. This work has focused particularly on the precision measurement of the radiative width of the Higgs, the study of heavy neutral Higgs bosons, and on detailed studies of supersymmetric particles and the top quark. The $\gamma\gamma$ channel is also highly sensitive to new physics such as large extra dimensions and the appearance of strong gravity at the 10 TeV scale.

With the publication of the TESLA Technical Design Report (TDR) and the development of the NLC/JLC toward full conceptual design, it was appropriate therefore to bring the photon collider from its highly schematic state into parity with the mature design of the rest of the accelerator. A year ago, a team of scientists and engineers from LLNL, SLAC, and UC Davis along with a FNAL-Northwestern theory consortium began to develop a complete design that would be required for full incorporation in the future NLC Conceptual Design Report. This effort involved a tightly integrated effort of particle theory and modeling, accelerator physics, optics, laser technology and engineering. The guiding principle was to develop a design that was robust, relied on existing technology, involved a minimum of R&D, and posed the least risk. Considerations of elegance, power efficiency and cost, while not unimportant, were relegated to second place. A satisfactory design was also required to stay well away from compounding detector backgrounds, and to involve minimal modification to the existing Final Focus and detector geometries. While this is still

a work-in-progress, the conclusion of the study so far is that a photon collider can be built with confidence on existing technology, satisfying these guidelines and criteria. This chapter describes the principal physics drivers for the $\gamma\gamma$ IR, and the basic design and technologies to implement it.

2 Physics Studies at a $\gamma\gamma$ Collider

2.1 Production of Higgs bosons

Perhaps the most important physics that can be done at a $\gamma\gamma$ collider is in probing the properties of the Higgs boson(s). At such colliders the Higgs bosons of the SM and the MSSM can be singly produced as s-channel resonances through one-loop triangle diagrams. They will be observed in their subsequent decay to $b\overline{b}, \tau^+\tau^-, WW^*, ZZ$, *etc.* Contributions to this type of loop graph arise from all charged particles that receive mass from the produced Higgs. In the SM, the loop contributions are dominated by the W and top. SUSY contributions may be as large as 10% of the SM amplitude. In addition, other currently unknown particles may also contribute to the loop and their existence may be probed indirectly by observing a deviation from the SM value. (Since other particles, such as gravitons, can also appear in the s-channel, it will also be necessary to determine the spin of any resonances that are produced.) By combining measurements at both e^+e^- and $\gamma\gamma$ colliders it will be possible to determine both the quantity $\Gamma_{\gamma\gamma}$ and the Higgs total width [3,4].

A light Higgs ($m_H \leq 135$ GeV) can be detected in the $b\overline{b}$ mode, with the main background due to the conventional QED $\gamma\gamma \to b\overline{b}, c\overline{c}$ continuum [3,4]. Because of the relatively large $c\overline{c}$ cross section, excellent b tagging is necessary. The two initial photon polarizations can be chosen to produce spin-zero resonant states and to simultaneously reduce the cross section for the background which, at tree level, is suppressed by m_q^2/m_h^2. Unfortunately, both QCD and QED radiative corrections remove this strong helicity suppression and must be well accounted for in both the Higgs and QED channels when comparing anticipated signals and backgrounds. Several detailed Monte Carlo simulations have been performed for this channel, with some typical results shown in Fig. 13.1 [5]; these have demonstrated that the quantity $\Gamma_{\gamma\gamma}B(h \to b\overline{b})$ can be determined with a relative error of 2%. Assuming that the $b\overline{b}$ branching fraction can be measured to the level of 1% by combining e^+e^- and $\gamma\gamma$ data, $\Gamma_{\gamma\gamma}$ will be determined at the level of 2%. This level of accuracy is sufficient to distinguish the SM and MSSM Higgs and to see contributions of additional heavy states to the triangle loop graph. If e^+e^- colliders can also provide the branching fraction for $h \to \gamma\gamma$ at the $\sim 10\%$ level, the total Higgs width can be determined with a comparable level of uncertainty. A similar analysis can be performed using either the WW^* or ZZ final state for Higgs masses up to 350-400 GeV, with comparable results [4].

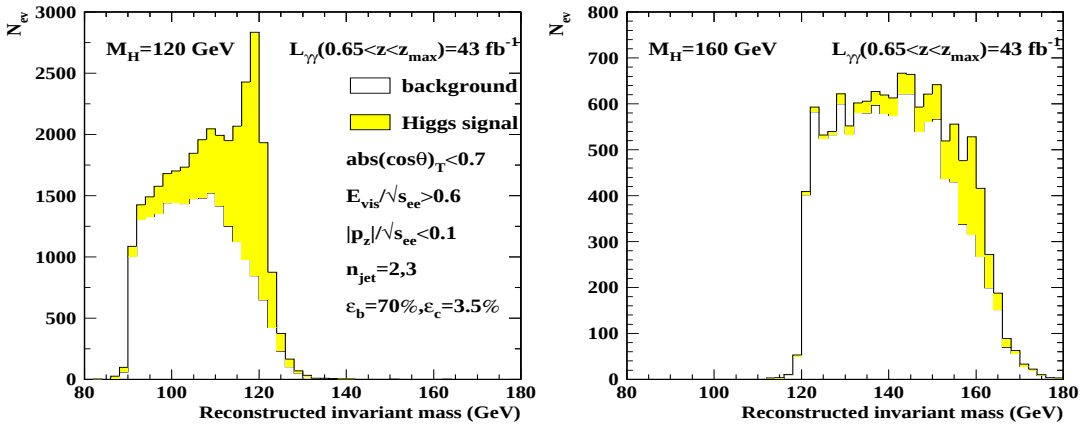

Figure 13.1: Mass distributions for the Higgs signal and heavy quark background for a Higgs mass of 120(left) and 160(right) GeV from Söldner-Rembold and Jikia [5]. The reduced signal-to-background at 160 GeV reflects the diminished branching ratio to $b\overline{b}$ near the WW threshold.

Very heavy Higgs bosons, such as those present in the MSSM, can also be produced as s-channel resonances in $\gamma\gamma$ collisions. In the MSSM, these heavy states have suppressed couplings to gauge bosons and may be most easily observed in $b\overline{b}$ or $t\overline{t}$ final states. These states may escape discovery at the LHC for intermediate values of $\tan\beta$. At e^+e^- colliders they can only be produced via associated production, $e^+e^- \to HA$, and thus lie outside the kinematic reach of the machine if their mass exceeds 240 GeV. The single production mode of the $\gamma\gamma$ collider allows the discovery reach to be extended to over 400 GeV. The $\gamma\gamma$ collider also allows one to separate degenerate H and A states and to study possible CP-violating mixing between H and A using linear polarization.

2.2 Supersymmetric particle production

For production significantly above threshold, sfermion and charged Higgs boson pairs have production cross sections in $\gamma\gamma$ collisions that are larger than those in e^+e^- annihilation. Thus, $\gamma\gamma$ collisions can provide an excellent laboratory for their detailed study. In addition, $\gamma\gamma$ production isolates the electromagnetic couplings of these particles, whereas in e^+e^- the Z and possible t-channel exchanges are also present. Thus complementary information can be obtained by combining data extracted from the two production processes. It should be noted that the search reach for new particles is typically somewhat greater in e^+e^- because of the kinematic cut-off of the photon spectra. However, the SUSY process $\gamma e \to \tilde{e}_{L,R}\chi_1^0$ shows that there are exceptions to this rule; the threshold for this process can be significantly below that for $\tilde{e}$ pair production in e^+e^- collisions when the χ_1^0 is light. In the study of this reaction, both the $\tilde{e}$ and χ_1^0 masses can be determined.

2.3 $\gamma\gamma \to W^+W^-$ and $\gamma e \to W\nu$

New physics beyond the SM can affect the expected values of the trilinear and quartic couplings of gauge bosons. These couplings can be studied in the reactions $\gamma e \to W\nu$ and $\gamma\gamma \to WW$, as well as in $e^+e^- \to WW$ [6]. It is noteworthy that the photon collider reactions isolate the anomalous photon couplings to the W, while $e^+e^- \to WW$ also involves anomalous Z couplings. In addition, the process $\gamma\gamma \to W^+W^-$ allows access to the quartic $\gamma\gamma W^+W^-$ coupling. The complementarity of the three reactions in determining the anomalous couplings is illustrated in Fig. 13.2, taken from [6]. Since the time of this study, it has been understood how to achieve bounds on the anomalous couplings from $e^+e^- \to WW$ that are a factor of 30 better than those shown in the figure, by taking advantage of more systematic event analysis and higher luminosities. Methods for that analysis are described in Chapter 5, Section 2. A similar improvement should be possible for the constraints from $\gamma e \to W\nu$ and $\gamma\gamma \to WW$, though the detailed study remains to be done.

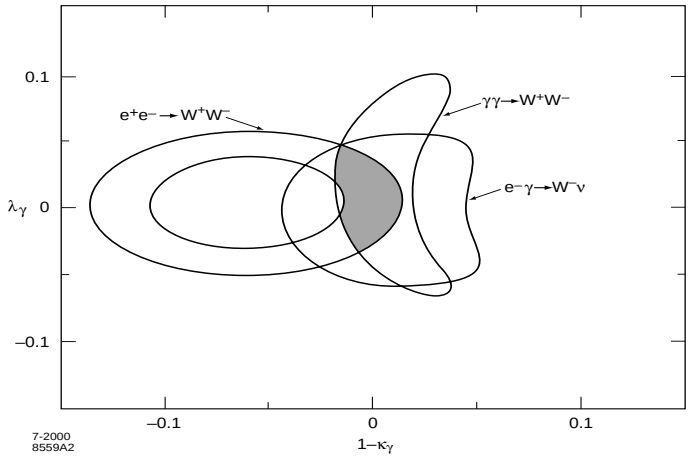

Figure 13.2: Allowed overlapping regions in the $\Delta\kappa_\gamma - \lambda_\gamma$ anomalous coupling plane, from the analysis of Choi and Schrempp [6].

The reaction $\gamma\gamma \to W^+W^-$ is also highly sensitive to other forms of new physics such as the exchange of virtual towers of gravitons that occurs in models of millimeter-scale extra dimensions [7,8]. It has been shown that this is the most sensitive process to graviton exchange of all those so far examined. Such exchanges can lead to substantial alterations in cross sections, angular distributions, asymmetries and W polarizations. These effects make it possible to probe the associated gravitational mass scale, M_s, to values as high as $13\sqrt{s}$ for the correctly chosen set of initial laser and electron polarizations. (For comparison, the reach in e^+e^- is about $7\sqrt{s}$.) The search reach as a function of the $\gamma\gamma$ luminosity is shown in Fig. 13.3 for the various

polarization choices. This same process can be used to search for graviton resonances such as those predicted in the Randall-Sundrum model [9].

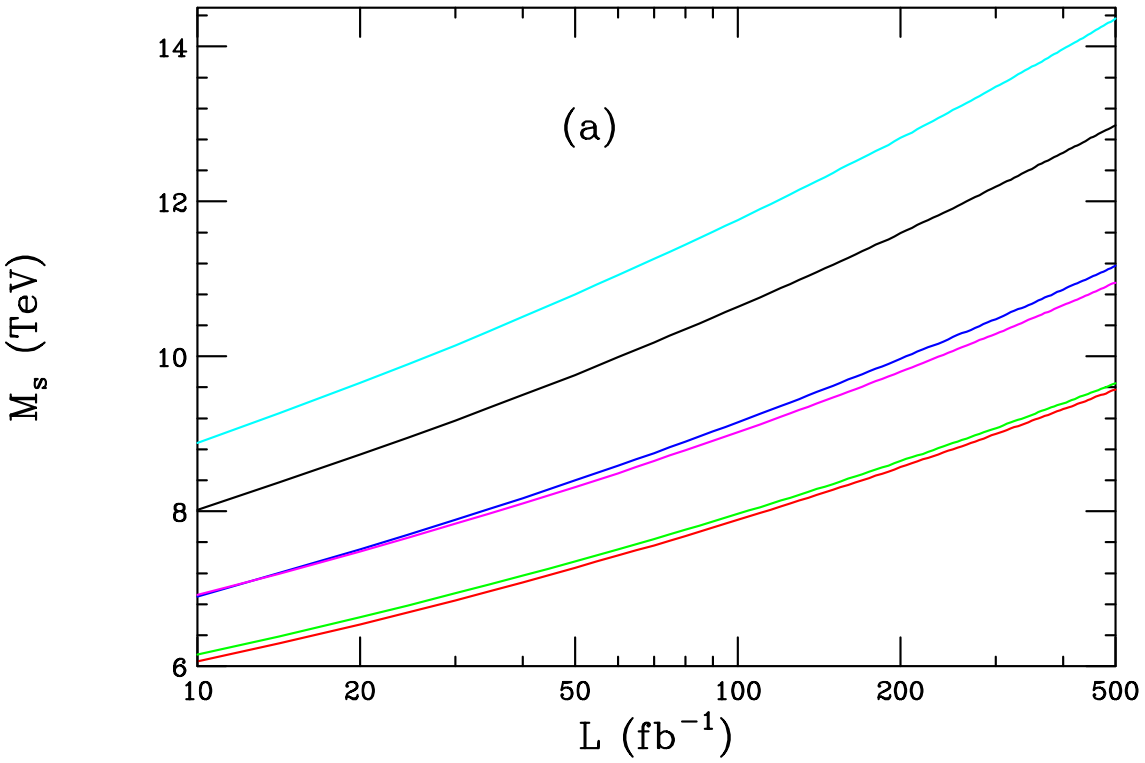

Figure 13.3: M_s reach for the process $\gamma\gamma \to W^+W^-$ at a 1 TeV e^+e^- collider as a function of the integrated luminosity for the different initial and final state polarizations. From top to bottom on the right hand side of the figure the polarizations are $(-+\,+-)$, $(+-\,--)$, $(++\,--)$, $(+-\,+-)$, $(+-\,--)$, and $(++\,++)$.

2.4 $\gamma\gamma \to t\bar{t}$

Since the top quark is the heaviest SM fermion, with a Yukawa coupling that is quite close to unity, one might expect that its properties may be the most sensitive to new physics beyond the SM. For example, the top may have anomalous couplings to the SM gauge bosons, including the photon. The cross section for top pairs in $\gamma\gamma$ collisions is somewhat larger than in e^+e^-, thus this process may provide the best laboratory to probe new physics couplings to the top. In addition, while both e^+e^- and $\gamma\gamma$ colliders can probe the anomalous $\gamma t\bar{t}$ couplings, these are more easily isolated in $\gamma\gamma$ collisions. As shown in [10], there are 4 form factors that describe this vertex, one of which is CP-violating and corresponds to the top quark electric dipole moment. By measurements of the $t\bar{t}$ angular distribution significant constraints on these form

factors are possible with sensitivities to both electric and magnetic dipole moment couplings that are about an order of magnitude better in $\gamma\gamma$ colliders than in e^+e^- machines. In addition, CP-violating couplings can be directly probed through the use of polarization asymmetries and limits superior to those obtainable from e^+e^- colliders are possible.

2.5 Other processes

There are many other interesting processes that one can study in $\gamma\gamma$ collisions. As far as new physics is concerned, the $Z\gamma$ and ZZ final states can be used to probe anomalous $ZZ\gamma$ and $Z\gamma\gamma$ couplings [11] while the $\gamma\gamma$ final state can be used to search for non-commutativity and violations of Lorentz invariance in QED [12]. The couplings of leptoquarks discovered in e^+e^- collisions can be more easily disentangled by using data from both $\gamma\gamma$ and γe collisions [13]. It may also be possible to form resonances of stoponium, the supersymmetric version of toponium, with production rates that are significantly higher than in e^+e^- [14].

Within the SM there are a number of interesting QCD processes that can also be examined to obtain information on topics such as the gluon and quark content of the photon, the spin-dependent part of the photon structure function, and the QCD pomeron. These topics are reviewed in Chapter 7, Section 3.

3 Compton Backscattering for $\gamma\gamma$ Collisions

3.1 Introduction

High-energy photons can be produced through two-body scattering of laser photons from a high-energy electron beam. For example, the scattering of 1 eV laser photons from an electron beam of 250 GeV can produce gammas of up to 200 GeV. An electron linear collider can be converted to a $\gamma\gamma$ collider if a high-power laser pulse intersects the electron beam just before the interaction point (IP). The point where the laser beam intersects the electron beam—the conversion point (CP)—can be within 1 cm of the IP. A high $\gamma\gamma$ luminosity comparable to that of e^+e^- can be achieved, since the photons will focus to about the same spot size as the electron beam. The principles are reviewed in detail elsewhere [15].

3.2 Photon spectra

For the case mentioned above—1 eV laser photons and 250 GeV electrons—the energy spectrum of the backscattered photons ranges from 0 up to 0.8 of the incoming beam energy. Two-body kinematics creates a correlation between the photon energy and the angle between the outgoing photon and the incoming electron. The maxi-

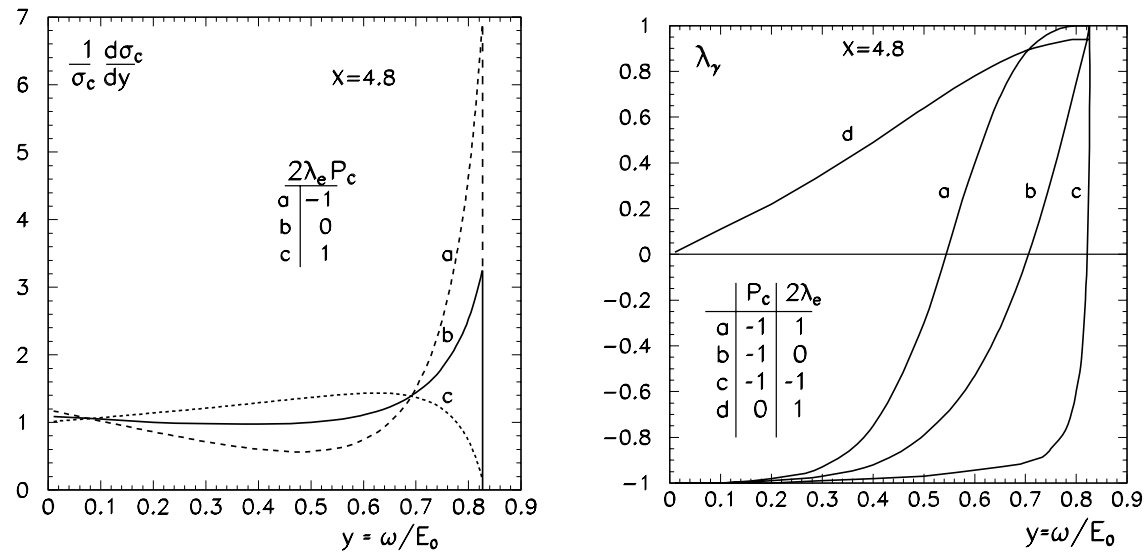

Figure 13.4: The energy spectrum and helicity spectrum of the Compton-backscattered photons for various helicities of the incoming electron beam with circularly polarized incoming photons [15]. The variable y is the photon energy as a fraction of the electron beam energy. The laser photon and electron helicities are designated by P_c and λ_e. The parameter $x = 4E_e\omega_0/m^2c^4$.

mum photon energy occurs when the produced photon is collinear with the incoming electron.

The exact energy spectrum is a function of the polarization of the incoming electron and laser beams. Figure 13.4 shows the energy spectrum of the backscattered photons for circularly polarized laser photons. The population of the high-energy peak is maximized when the electron beam is fully polarized and of opposite helicity to the laser beam. For that situation, the high-energy photons are also fully circularly polarized. While the lasers naturally produce linearly polarized photons, any combination of circular and linear polarization can be produced through the use of quarter-wave plates.

From Fig. 13.4 it can be seen that the ability to polarize the incoming electron beam is crucial for producing high-energy $\gamma\gamma$ collisions with polarized gammas. Currently it is foreseen that the electron beams will achieve 80% polarization while positrons will be unpolarized. This makes it attractive to run in an e^-e^- mode rather than e^+e^-. Many Standard Model backgrounds are also suppressed by choosing e^-e^- running.

Calculating the $\gamma\gamma$ luminosity spectrum at the IP is not as simple as convoluting the single-scattering energy spectrum with itself. There are additional sources of γ's that must be included. An electron can Compton backscatter multiple times as it

passes through the laser beam. This leads to a tail of low-energy photons, as can be seen in Fig. 13.5. Also, the leftover electron beam arrives at the IP coincident with the photons. When the two electron beams interact they produce a large number of beamstrahlung photons. All of these contribute to the $\gamma\gamma$ luminosity.

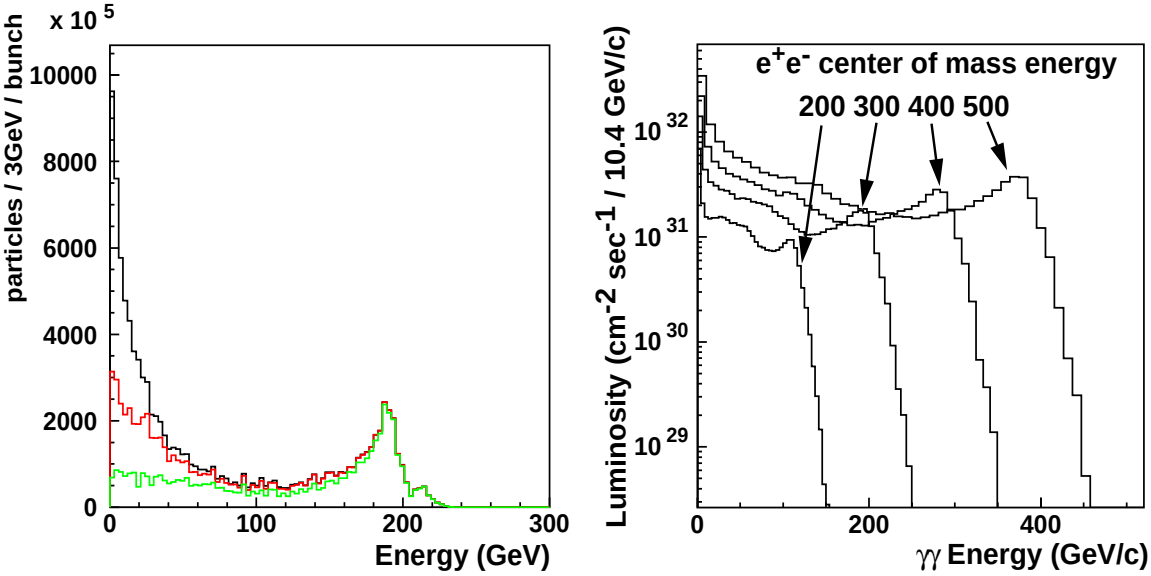

Figure 13.5: The first plot shows the energy spectrum from Compton backscattering when (respectively, from the bottom curve to the top) primary, secondary, and all higher scatters are taken into account. The second plot shows the $\gamma\gamma$ luminosity for e^-e^- center-of-mass energies of 500, 400, 300, and 200 GeV for the NLC-B machine parameters.

As a result of the energy-angle correlation, the spot size for collision of soft photons will be larger than that for the collision of harder photons. Thus the luminosity spectrum may be hardened by increasing the distance between the CP and IP. In the following, we chose the CP to be 5 mm from the IP.

To compute the $\gamma\gamma$, $e\gamma$ and ee luminosities, we use the program CAIN [16], which models all of the processes just described. Results for various incident electron beam energies are shown in Fig. 13.5. The luminosity spectrum peaks at $\gamma\gamma$ CM energies close to 0.8 times of the e^-e^- CM energy. The decrease of luminosity with decreasing CM energy, apparent from the plot, is primarily caused by the increased spot size of the electron beams and, secondarily, by a softer Compton-backscattering spectrum. For a 120 GeV Higgs this leads to a situation where higher luminosities can be achieved by running at 500 GeV e^-e^- CM energy at the cost of having unpolarized photons. For measurements requiring definite states of $\gamma\gamma$ polarization, on-peak running with 150 GeV e^-e^- CM energy is required.

3.2.1 Accelerator modifications

While no changes to the accelerator are required to produce $\gamma\gamma$ collisions, some changes can optimize performance. Beam-beam interactions are a major concern for e^+e^- but are not present in $\gamma\gamma$ collisions. Therefore the β functions of the Final Focus should be as small as possible to achieve a minimum spot size and maximum luminosity. The luminosity improvements from small β functions are limited by chromatic aberrations in the Final Focus and the hourglass effect, in which the β function becomes comparable to the longitudinal spot size. In addition, a small transverse spot size tends to select unboosted events because of the correlation between the energy and production angle of the high-energy γ's. A Final Focus design with rounder beams simplifies the final doublet stabilization and has been shown to recover nearly a factor of two in luminosity by increasing the contribution of boosted events. However, these boosted events suffer from reduced reconstruction efficiency and we have not yet optimized the design for this effect.

Achieving rounder beams requires only a change in the strength of the Final Focus magnets. It is useful also to cut the number of bunches in half and double the bunch charge, to better match the laser technology. This nominally increases the luminosity by a factor of two, although this is not fully achieved due to the increased emittance growth and the increased longitudinal spot size. The parameters we use are shown in Table 13.1. These have been reviewed and approved by the NLC machine group. When we reduce the e^-e^- CM energy such that the $\gamma\gamma$ peak is at 120 GeV for Higgs running, the $\gamma\gamma$ luminosity becomes 2.9×10^{31} cm^2/s/GeV at $\sqrt{s_{\gamma\gamma}} = 120$ GeV, with 80% of events being spin 0.

e^-e^- CM Energy (GeV)	490
Luminosity	1.23×10^{33} @ >65% e^-e^- energy
Bunch Charge	1.5×10^{10}
Bunches / pulse	95
Bunch separation	2.8 ns
$\gamma\epsilon_x$ at IP	360×10^{-8} m-rad
$\gamma\epsilon_y$ at IP	7.1×10^{-8} m-rad
β_x / β_y at IP	0.76/1.81 mm
σ_x / σ_y at IP	76/16 nm
σ_Z at IP	0.150 mm

Table 13.1: NLC-G parameter set. Unless otherwise noted parameters are identical to NLC-H.

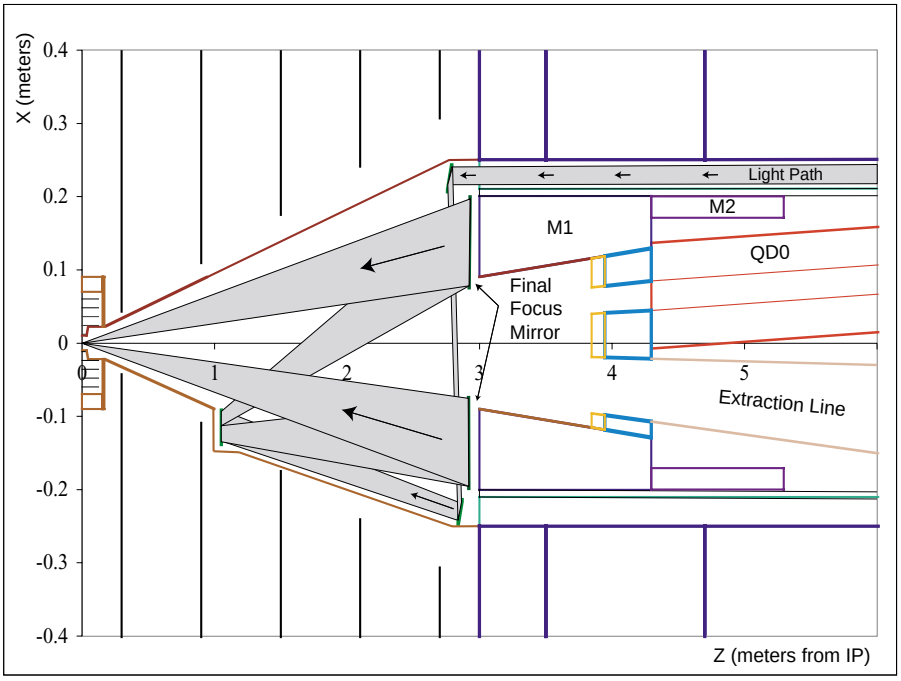

Figure 13.6: Optical configuration to inject the laser light into the Interaction Region. The high subpulse intensity requires all these optics to be reflective and mounted inside the vacuum enclosure.

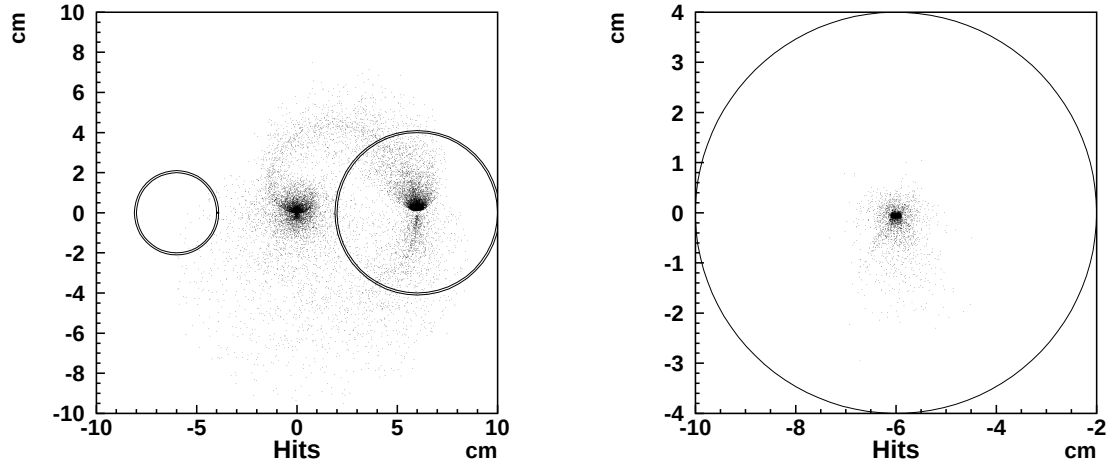

Figure 13.7: The front face of the magnet at $z = 4$ meters. The first plot shows the impact point of the pair background. High-energy particles travel out the extraction line. Low-energy particles spiral in the solenoidal magnetic field of the detector. The second plot is an expanded view of the extraction line aperture showing the location of the outgoing beam.

3.3 Interaction region design and backgrounds

Figure 13.6 shows the interaction region for a $\gamma\gamma$ collider. The design begins from the IR for e^+e^- collisions, but many modifications are needed to accommodate the laser beams. The first of these is the system of mirrors required to bring laser light into the IR, described in detail in Section 4.1. The mirrors have been carefully placed to be outside the path of the beams and the pair background. The pair background consists of low-energy electrons and positrons which spiral in the magnetic field of the detector. Their transverse location at $z = 4$ meters can be seen in Fig. 13.7. No additional backgrounds are generated by the presence of the mirrors.

The extraction lines for the spent beams must be modified for the $\gamma\gamma$ interaction region. The energy spectrum of electrons leaving the conversion point is composed of unscattered electrons at the beam energy and scattered electrons which peak around 1/5 the beam energy. The low-energy electrons receive a larger angular deflection from the beam-beam interaction at the IP, necessitating an increased aperture for the extraction line. Additionally, just as in the case of the pair background, the low-energy electrons spiral in the magnetic field. Figure 13.7 shows the position of the outgoing electrons at the entrance to the extraction line. An aperture of ± 10 milliradians accommodates these particles. In order to prevent mechanical interference between the extraction line and the last focusing quadrupole, the crossing angle has been increased from 20 to 30 milliradians.

Increasing the extraction line aperture has a detrimental effect on the neutron background levels at the IP. The Silicon Vertex Detector, 1.2 cm away from the IP, now has a direct line of sight back to the beam dump 150 meters away. It experiences a fluence of 10^{11} neutrons/cm^2/year. The standard CCD technology chosen for the e^+e^- IR cannot withstand it. The $\gamma\gamma$ IR would need a rad-hard CCD or pixel design.

We foresee no impact to the detector aside from the need for a rad-hard vertex detector. The machine backgrounds in the $\gamma\gamma$ IR are comparable to the e^+e^- IR. Still to be evaluated is the effect of resolved photon events from the higher $\gamma\gamma$ luminosity.

4 IR optical system

4.1 Optics design

The function of the optical system is to bring the laser beam to the IR while also minimizing the required laser pulse energy. The requirement for efficient conversion of the electrons sets the laser photon density required at the interaction point. The optical system will focus the laser beam at a point near the interaction point to maximize the conversion probability. The size of the laser focal spot will be much larger than the electron beam; therefore the size of the focal point should be minimized in order to minimize the required laser pulse energy.

When bringing a beam to a focus, the size of the focal point is determined by the f-number of the focusing optic, defined as the ratio of the focal length to the optic diameter. The size of the useful laser spot is approximately the wavelength times the f-number. There is a limit, however, to how small one can usefully make the f-number. The focal spot has a limited depth of focus. When the electron-photon interaction region becomes longer than the depth of focus, the required laser energy becomes independent of the f-number. Lowering the f-number beyond this point results in no decrease in the required laser pulse energy. Optimally, the laser pulse length should be the same as the electron bunch length to minimize the required pulse energy. However, at such high intensities, non-linear effects degrade the purity of the photon polarization. We choose a pulse length of 2 ps FWHM, which is well matched to the available laser technology. For such a 2 ps laser pulse, decreasing the f-number below 7 gains little further energy reduction. For the reference design the f-number is 8.

Figure 13.6 shows the optical design near the interaction region. The final focusing optic is located at the 3 m station and is mounted adjacent to (or on) the 40 cm diameter tungsten plug (M1). The optic has a 300 cm focal length and a 38 cm diameter, giving it an f-number of 8. The central 15 cm hole provides a space for the electron beams and high-energy scattered electrons to pass through the Final Focus optic. The secondary optic is mounted off-axis to minimize the obscuration of the laser beam. Additional turning optics provide centering and pointing capabilities as well as beam injection to the secondary optic. The high subpulse intensity requires all these optics to be reflective and mounted inside the vacuum chamber.

The laser beam enters the IR from one side. A symmetric set of optics (not shown in Fig. 13.6) takes the beam to a mirror that sends the beam back to a focus intersecting the second electron beam. The difference in the image plane of the focal spots as well as the difference in arrival times can then be used to separate the incoming and exiting laser beams in the beam transport system.

4.2 Beam pipe modifications

The short pulse format of the laser results in beam intensities that cannot be propagated through air or transmissive optics. The pulse compression, beam transport and IR injection optics will all be reflective optics inside vacuum enclosures. The small vacuum pipe that transports the electron beam must be expanded in the IR to contain the laser injection optics (as shown in Fig. 13.6). The level of vacuum required will be determined by the electron beam since it will be higher than needed by the laser. It should be noted that the vacuum requirement of the electron beam may place restrictions on the materials that can be used in the optics mounts and controls.

The laser beam transport pipe will contain isolation gate valves that will be open when the laser is operating. These valves can be closed during maintenance and

other operations when the laser in not operating. They can also be used to prevent contamination or accidental pressurization of the linac and IR during shutdowns.

The optics and vacuum enclosures will be mounted on the same structures as the electron beam transport system. The electron beam transport system in the IR region has not been designed in sufficient detail to begin the design of the laser system interfaces. The seismic requirements for the laser optics are not as stringent as for the Final Focus magnets. If both systems use the same supports, it will be important that the laser system does not feed excessive acoustic energy into the final quadrupole support structure.

5 Laser system

5.1 Requirements and overview

The laser system must match the pulse format of the electron beam and supply an adequate photon density at the IR to backscatter the laser photons efficiently to gamma rays. For efficient conversion of 250 GeV electrons, the optimal laser wavelength is one micron. The laser requirements for the NLC are summarized in Table 13.2.

A picosecond-duration laser pulse cannot be amplified to the joule level directly. The combination in the laser subpulse of a high pulse energy (1 J) and a short pulse duration (2 ps) generates field intensities that will damage laser materials. This problem is solved by first stretching a very low-energy laser subpulse to 3 ns and then amplifying this long pulse. The pulse is then compressed back to 2 ps for use in the IR. The procedure for stretching and compressing the laser pulse with diffraction gratings, known as Chirped-Pulse-Amplification (CPA) [17], is discussed below. The procedure requires the laser medium to have significant gain bandwidth.

Efficiently energizing a laser with the very low required duty factor (300 ns/8 ms) requires the use of a 'storage laser' material. Generally storage lasers are solid-state and, when used in a high-pulse-rate application, they are strongly limited by heat-removal capabilities. LLNL has been developing a solid-state Yb:S-FAP laser with diode pump lasers and rapid helium gas cooling to address this issue as part of its Inertial Fusion Energy program. The Mercury Laser Project is currently assembling a prototype. The default Mercury laser pulse format differs from that required for $\gamma\gamma$ operation. The necessary modifications of the laser are described below.

5.2 Laser system front end

The laser system front end must generate a low-power laser signal with a temporal format matched to that of the electron linac. This signal will then be delivered to the Mercury amplifiers to generate the high pulse energies needed to interact with the electron pulses.

A laser oscillator will be required with an approximately 350 MHz pulse rate and 2 ps pulse duration. With pulse energies of 1.0 nJ, the average power will only be only 0.35 W. The laser must be tuned to the 1.047 micron wavelength which overlaps the gain bandwidth of the Yb:S-FAP laser amplifiers. Commercial Ti-sapphire lasers will be appropriate for this task. The laser oscillator must have high frequency stability and must be locked to the master clock of the linac so that the laser pulse timing matches that of the electron pulses.

The beam from the oscillator will pass through a Pockels cell slicer that will cut out 300 ns pulse trains at 120 Hz. These batches will match the electron bunch trains, which contain approximately 100 subpulses. The pulse trains will then be passed through an electro-optic modulator that will impose a moderately increasing amplitude ramp on the macro-pulse. This amplitude ramp is designed to offset the decreasing gain ramp that will be experienced in the amplifier as the stored energy is extracted during the laser macro-pulse. The low power (about 1 μW) is easily handled by current EO modulators.

The gain in the amplifier will have frequency variations as well as amplitude diminution during the macro-pulse. To avoid strong amplitude variations at different frequencies in the amplified laser signal, the amplitude of the input laser beam will be sculpted in frequency space [18] to offset the effects of the gain variation. The short pulse length of the subpulses gives them a frequency bandwidth such that a diffraction grating will spread the beam over a range of angles. The different frequencies are then passed through a programmable liquid crystal display that provides different attenuation for different positions (frequencies) in the beam.

The laser beam is next passed through a diffraction grating pulse stretcher, described in a later section, that stretches the 2 ps subpulses to 3 ns. The spectral sculpting and pulse stretching might be combined into a single device if appropriate.

The stretched laser pulses can now be passed through a high-gain, low-power preamplifier. A laser optical parametric amplifier (OPA) will provide the high bandwidth needed to preserve the frequency profile of the laser pulse. A high-pulse energy green laser will pump a BBO crystal to provide the gain needed. The laser beam will be amplified to 500 μJ/subpulse. The beam will be split into twelve 10 Hz beams and then injected into the Mercury amplifiers.

Wavelength	1 μ	Format	$\sim$ 100 subpulses/macro-pulse
Subpulse energy	1 J	Repetition rate	120 Hz
Subpulse separation	2.8 ns	Gain bandwidth	10 nm
Subpulse duration	2 ps	Beam quality	$<$ 1.5 diffraction limit

Table 13.2: $\gamma\gamma$ collider laser requirements.

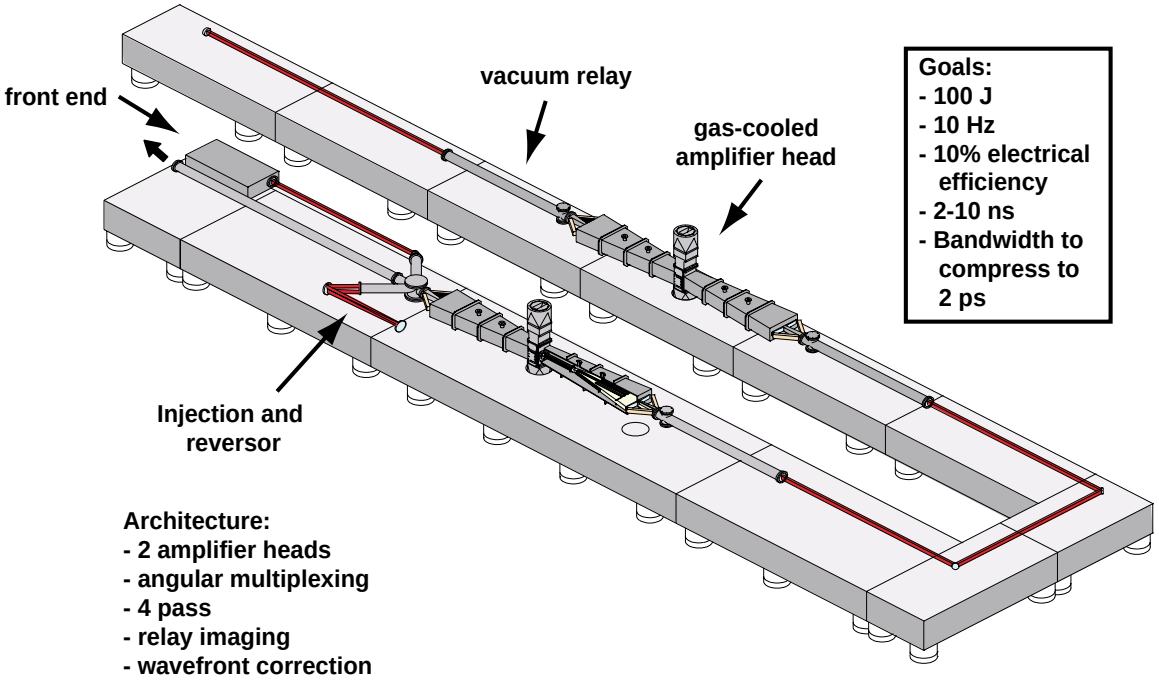

Figure 13.8: The diode-pumped solid state Mercury laser is a high-pulse rate, next-generation laser fusion driver.

5.3 Mercury amplifier

The Mercury laser (Fig. 13.8) will operate at 10 Hz with 100 J pulses. Twelve such lasers would have to be time-multiplexed to achieve the $\gamma\gamma$ laser requirements. The major challenge will be the modification of the Mercury laser pulse format, which is currently a single several-nanosecond-long pulse. Achieving the desired diffraction-limited beam quality will also be an important challenge.

The Mercury laser utilizes three primary innovations to achieve the goal of a high-efficiency, high-repetition-rate laser driver for laser fusion experiments. The first is that the removal of heat from the laser media is accomplished by flowing helium at high speed over the surface of thin laser slabs. The thermal gradients in the laser media are oriented both in the short dimension, for effective conductive cooling, and in the direction of the laser propagation, to minimize the optical distortion. The low index of refraction of helium minimizes the helium thermal-optical distortions that must later be removed with adaptive optics. Figure 13.9 shows the arrangement of thin laser slabs embedded in flow vanes within the helium flow duct. Full-scale demonstrations have validated the flow and thermal models have confirmed that the design meets the optical system requirements.

The second innovation is the use of diode lasers rather than flash lamps to energize

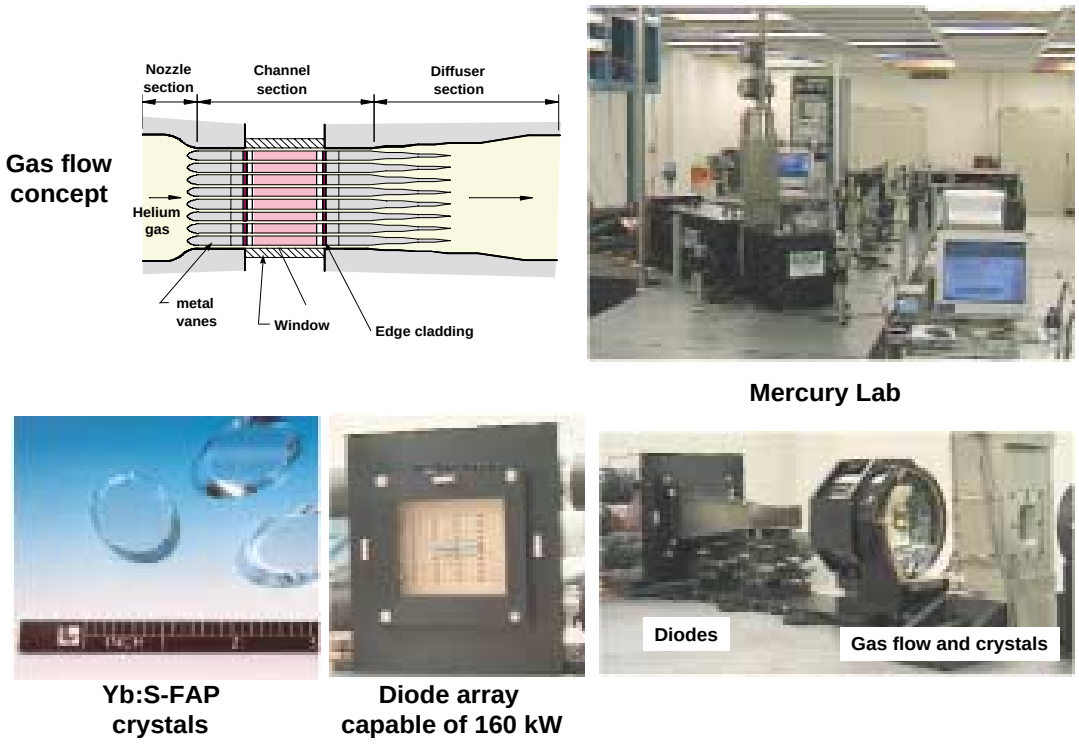

Figure 13.9: The Mercury laser will utilize three key technologies: gas cooling, diodes, and Yb:S-FAP crystals to deliver 100 J at 10 Hz with 10% efficiency.

the laser media. The narrow frequency output of the diode laser is matched to the absorption band of the laser media. The efficient coupling and the efficiency of diode lasers result in significantly higher pumping efficiency of the laser media and also significantly lower waste heat that must be removed by the helium cooling system. The primary challenge for the diode laser design is minimizing the high capital cost of the diode laser and its packaging design. LLNL has developed a low-cost packaging design that also efficiently couples the diode light into the laser slabs. This design has been produced under commercial contract and will be tested this year in the Mercury laser laboratory.

The third innovation is the use of Yb:S-FAP as the laser media instead of the usual Nd-glass. This crystalline media has better thermal conductivity for cooling, longer storage lifetime for efficient pumping, and a high quantum efficiency to minimize waste heat. The growth of these new crystals (Fig. 13.9) with adequate size and optical quality has been the primary technical challenge in the Mercury project. Crystals

grown recently may satisfy these requirements, but some testing remains to be done.

The Mercury laser has two amplifier heads and a four-pass optical system. This year one amplifier head and the full optical configuration will be tested in the Mercury laboratory. A second amplifier head must be constructed before full-power extraction can be demonstrated.

5.4 Multiplexer and beam transport

The beams from twelve Mercury lasers, each operating at 10 Hz, must be combined into a single co-aligned beam to produce the required 120 Hz beam. The beam combination should occur before the pulse compressor to minimize the stress on the combiner optics. At these low pulse rates the simplest beam combination scheme is a simple rotating faceted optic.

The beam combination optic is a 4 cm-diameter optic with twelve flat facets each covering a thirty degree sector. Each facet is ground at a slightly different angle. The optic is rotated on its axis at 10 Hz (600 rpm). The twelve incoming laser beams arrive at slightly different angle, such that they are all aligned after reflection off the optic. The angle differences are sufficiently large to allow the incoming laser beams to be projected from spatially separated optics. The incident laser beam diameter of 0.5 cm will give a power density of 5 kW/cm^2 on the optic. This will be below the damage threshold of 10 kW/cm^2. The optic can be made larger if a larger damage margin is desired.

The combined beam is then transported to the pulse compressor. The pulse compressor can be located in the laser facility or close to the detector, just prior to the final transport optics into the IR. For the reference design it is assumed that the compressor is located in the laser facility and that the laser facility is located a nominal 100 meters from the detector hall. The transport of the laser beams will be in vacuum pipes from the exit of the Mercury laser modules. To minimize the evolution of amplitude variations due to diffraction or phase aberrations, the laser beam will be expanded to a nominal 10 cm and image-relayed. The vacuum tubes should be 15 cm to allow for errors in initial alignment procedures.

5.5 Compressor / stretcher

The basic concept of compressing long pulses into short pulses after amplification is well known and widely used [19,20]. The challenge is in designing and fabricating high-efficiency gratings that can handle high-power laser beams. The specifications for the stretcher and compressor systems are given in Table 13.3.

The subpulses from the oscillator are 2 ps and 1.0 nJ. Their transform-limited full-width-half-maximum is 0.9 nm. The gratings in the stretcher give the beam an angular spread. Light of different wavelengths within the bandwidth of the laser follows optical paths of different length, thus introducing a frequency-time correlation

	Stretcher	Compressor
Substrate material	silica	silica
Coating material	gold	Multi-layer
First grating size (cm)	4 x 15	30 x 84
Second grating size (cm)	4 x 15	30 x 84
Roof mirror size (cm)	4 x 8 (flat)	30 x 40
Grating separation (m)	5	15
Lines per mm	1740	1740
Laser beam diameter (cm)	1	10
Cut bandwidth (nm)	2.0	2.0
Exit subpulse duration (ps)	3000	2.2
Efficiency-single bounce (%)	90.	96.0
System efficiency (%)	60	80
Laser macro-pulse fluence (J/cm^2)	10^{-7}	1.3
Damage fluence (J/cm^2)	0.4	2.0

Table 13.3: Specifications for stretcher and compressor optical systems.

to the subpulse ("chirping"). The laser subpulse has a 3 ns halfwidth duration upon exiting. The finite size of the grating results in the truncation of some frequencies and gives the exiting pulse a truncated spectral distribution and a temporal pulse with side lobes. The 100 subpulses that are separated by 2.8 ns will overlap to form a 300 ns macro-pulse that has some ($\sim 10\%$) time/amplitude modulation. Since the beam in the stretcher is of such low power, there are no technical issues with this system. The system efficiency will be limited by the reflectivity of the gratings in the first order and the frequency clipping due to finite grating size.

The compressor gratings must be designed to handle the full 100 J macro-pulses without damage. The 100 Hz pulse rate will also generate an average-power thermal concern. The large gold coatings used in laser fusion experiments (Fig. 13.10) have too large an absorption and would have thermal distortion problems. LLNL has also developed multi-layer dielectric diffraction gratings with high efficiency [21]. Their low absorptivity removes the thermal concerns while also increasing the system efficiency. Figure 13.10 shows the design of these gratings. Alternating layers of hafnia and silica are placed on the substrate to give a high-reflectivity, high-damage fluence coating. The grating is etched in the silica overcoating.

5.6 Laser facility, systems design and risk reduction

The general layout of the laser facility is shown in Fig. 13.11. The facility is dominated by the operating bays for the laser amplifiers and their utilities. The operating strategy will be to do no laser repairs in these operation bays. The laser

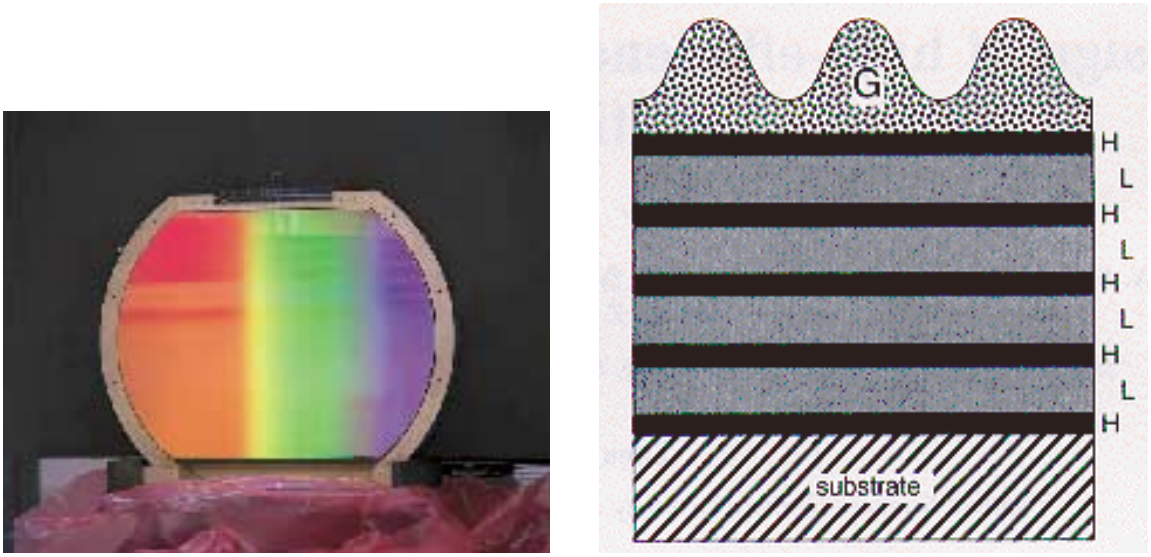

Figure 13.10: The 94 cm aperture gold-coated diffraction grating used for pulse compression on the Petawatt laser is shown on the left. A multilayer dielectric grating design of high-index (H) and low-index (L) layers and groove corrugations (G) is shown on the right. Layers form a high-reflectivity stack under the corrugations.

systems will be designed with quickly removable Line Replaceable Units (LRUs) for all the major subsystems, as in the NIF project. The equipment will be monitored by computer during operation. When a system needs special or preventive maintenance, the LRU is quickly removed and moved to a separate repair facility. A new LRU is inserted, and the laser is immediately returned to service. This repair strategy allows for high system availability without requiring excessive component lifetimes or redundancy. Some long-lifetime components such as the optics vacuum chamber may have to be occasionally repaired in place.

A systematic cost estimate has not yet been done. The expected capital cost is of order of $200M, and the operating budget of approximately $20M/yr. The largest uncertainties in the capital costs are the diode costs and the laser size needed to meet the performance requirements. The operating cost uncertainties are dominated by diode laser lifetime and cost uncertainties.

The cost risk reduction strategy is to identify the main cost drivers. Since diode lifetime is expected to be the primary cost risk driver, efforts will be made to acquire diode lifetime data.

The technical risks are dominated by the laser beam quality uncertainties and the lack of prototype demonstrations of some of the subsystems. The Mercury laser being built for the fusion program will serve as the main laser amplifier prototype. Other critical systems such as the laser system front end will be prototyped as part of a risk

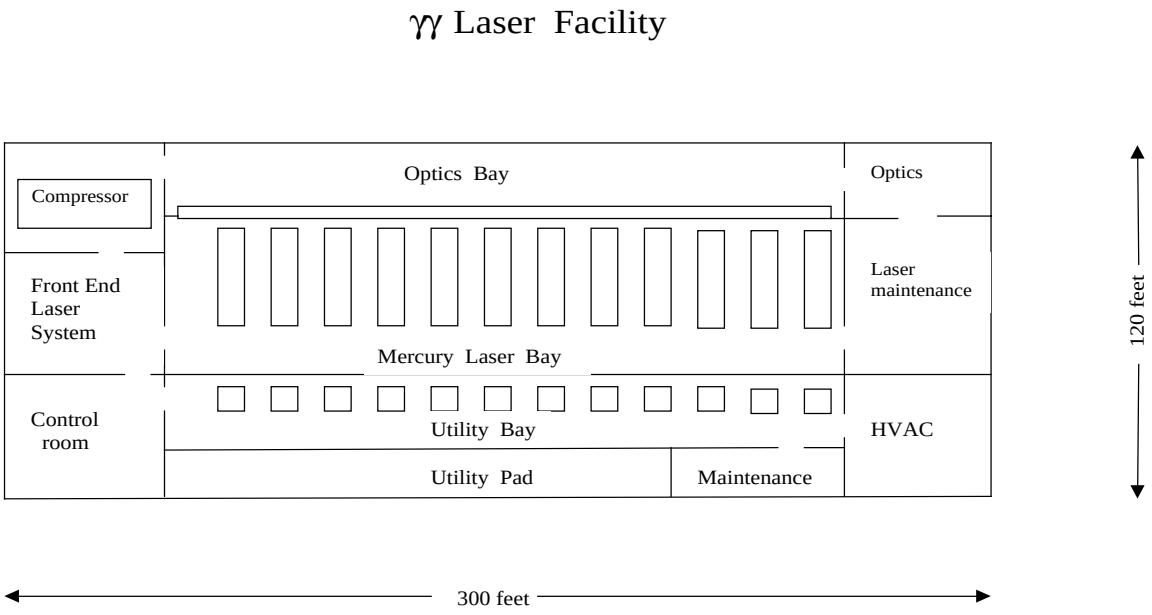

Figure 13.11: Floor plan of the laser physical plant.

reduction program.

References

[1] I. F. Ginzburg, G. L. Kotkin, V. G. Serbo and V. I. Telnov, Pizma ZhETF **34**, 514 (1981); JETP Lett. **34**, 491 (1982) (Preprint INF 81-50, Novosibirsk (1981) in English).

[2] I. F. Ginzburg, G. L. Kotkin, V. G. Serbo and V. I. Telnov, Nucl. Instrum. Meth. **205**, 47 (1983).

[3] D. L. Bordon, D. A. Bauer, and D. O. Caldwell, Phys. Rev. **D48**, 4018 (1993); T. Ohgaki, T. Takahashi and I. Wantanabe, Phys. Rev. **D56**, 1723 (1997); T. Ohgaki, T. Takahashi, I. Wantanabe and T. Tauchi, Int. J. Mod. Phys. **A13**, 2411 (1998); I. Wantanabe *et al.*, KEK Report 97-17 (1998).

[4] J. F. Gunion *et al.*, hep-ph/9703330; H. E. Haber, hep-ph/9505240; A. Djouadi, V. Driesen, W. Hollik and J. I. Illana, E. Phys. J. **C1**, 149 (1998); B. Grzadkowski and J. F. Gunion, Phys. Lett. **B291**, 361 (1992); J. F. Gunion and J. G. Kelly, Phys. Lett. **B333**, 110 (1994).

[5] See, for example, S. Söldner-Rembold and G. Jikia, in *Proc. Internat. Workshop on High-Energy Photon Colliders*, Hamburg, Germany, 14-17 June 2000; G. Jikia

and A. Tkabladze, Phys. Rev. **D54**, 2030 (1996); M. Melles, W. J. Stirling and V. A. Khoze, Phys. Rev. **D61**, 054015 (2000) and M. Melles, hep-ph/0008125; M. Battaglia, hep-ph/9910271.

[6] E. Yehudai, Phys. Rev. **D41**, 33 (1990) and **D44**, 3434 (1991); S. Y. Choi and F. Schrempp, Phys. Lett. **B272**, 149 (1991); S. J. Brodsky, T. G. Rizzo and I. Schmidt, Phys. Rev. **D52**, 4929 (1995); T. Takahashi, in *Physics and Experiments with Linear Colliders*, ed. A. Miyamoto *et al.* (World Scientific, Singapore, 1996); M. Baillargeon, G. Belanger and F. Boudjema, Nucl. Phys. **B500**, 224 (1997). For a review, see H. Aihara *et al.* in *Electroweak Symmetry Breaking and Beyond the Standard Model*, ed. T. Barklow *et al.*, (World Scientific, Singapore, 1996).

[7] N. Arkani-Hamed, S. Dimopoulos and G. Dvali, Phys. Lett. **B429**, 263 (1998) and Phys. Rev. **D59**, 086004 (1999); I. Antoniadis, N. Arkani-Hamed, S. Dimopoulos and G. Dvali, Phys. Lett. **B436**, 257 (1998); G. F. Giudice, R. Rattazzi and J. D. Wells, Nucl. Phys. **B544**, 3 (1999); T. Han, J. D. Lykken and R. Zhang, Phys. Rev. **D59**, 105006 (1999), E. A. Mirabelli, M. Perelstein and M. E. Peskin, Phys. Rev. Lett. **82**, 2236 (1999); J. L. Hewett, Phys. Rev. Lett. **82**, 4765 (1999); T. G. Rizzo, Phys. Rev. **D59**, 115010 (1999).

[8] T. G. Rizzo, Phys. Rev. **D60**, 115010 (1999).

[9] L. Randall and R. Sundrum, Phys. Rev. Lett. **83**, 3370 (1999). H. Davoudiasl, J. L. Hewett and T. G. Rizzo, Phys. Lett. **B473**, 43 (2000), hep-ph/0006041 and Phys. Rev. Lett. **84**, 2080 (2000).

[10] A. Djouadi, *Proc. of the Workshop on e^+e^- collisions at 500 GeV: the Physics Potential*, edited by P. Zerwas, DESY Report 92-123B; P. Poulose and S. D. Rindani, Phys. Lett. **B452**, 347 (1999); S. Y. Choi and Hagiwara, Phys. Lett. **B359**, 369 (1995); M. S. Baek, S. Y. Choi and C. S. Kim, Phys. Rev. **D56**, 6835 (1997).

[11] For a recent review and original references, see G. J. Gounaris, P. I. Porfyiadis and F.M. Renard, hep-ph/0010006.

[12] J. L. Hewett, F. J. Petriello and T. G. Rizzo, hep-ph/0010354.

[13] For a review, see A. Djoudai, J. Ng and T. G. Rizzo, in *Electroweak Symmetry Breaking and Beyond the Standard Model*, ed. T. Barklow *et al.*, (World Scientific, Singapore, 1996); W. Buchmüller, R. Rückl and D. Wyler, Phys. Lett. **B191**, 442 (1987); J. L. Hewett and T. G. Rizzo, Phys. Rev. **183**, 193 (1989) and Phys. Rev. **D56**, 5709 (1997); J. Blümlein and R. Rückl, Phys. Lett. **B304**, 337 (1993); S. Davidson, D. Bailey, and B. A. Campbell, Z. Phys. **C61**, 613 (1994); M. Leurer, Phys. Rev. **D50**, 536 (1994), and **D49**, 333 (1994).

[14] For a recent summary, see D. S. Gorbunov, V. A. Ilyin and V. I. Telnov, hep-ph/0012175.

[15] V. Telnov, Nucl. Instr. and Meth. **A 355**, 3 (1995).

[16] K. Yokoya, "A Computer Simulation Code for the Beam-Beam Interaction in Linear Colliders", KEK report 85-9, Oct. 1985.

[17] D. Strickland and G. Mourou, Opt. Commun. **56**, 219 (1985).

[18] M. D. Perry, F. G. Patterson, and J. Weston, Opt. Lett. **15**, 381 (1990)

[19] E. B. Treacy, IEEE J.Quantum Electron. **QE-5**, 454 (1969).

[20] M. D. Perry and G. Mourou, Science **264**, 917 (1994).

[21] B. W. Shore, M. D. Perry, J. A. Britten, R. D. Boyd, M. D. Feit, H. T. Nguyen, R. Chow, G. E. Loomis and Lifeng Li, J. Opt. Soc. Am., **14**, No.5, 1124 (May 1997).